npj | 2D Materials and Applications

www.nature.com/npj2dmaterials

Corrected: Publisher Correction

ARTICLE OPEN

Nitrogen-doping induces tunable magnetism in ReS_2

Qin Zhang[1], Zemian Ren[1], Nian Wu[1], Wenjie Wang[1], Yingjie Gao[1], Qiqi Zhang[1], Jing Shi[2], Lin Zhuang[1], Xiangnan Sun[3] and Lei Fu[1]

Transition metal dichalcogenides (TMDs) are promising for spintronic devices owing to their spin-orbit coupling and loss of inversion symmetry. However, further development was obstructed by their intrinsic nonmagnetic property. Doping TMDs with non-metal light atoms has been predicted to be a good option to induce unexpected magnetic properties which remain rarely explored. Here, we utilize nitrogen doping to introduce magnetic domains into anisotropic ReS_2, giving rise to a transition from nonmagnetic to tunable magnetic ordering. Both of the experimental and computational results confirmed that the N-doping in ReS_2 prefers to take place at the edge site than in-plane site. With controlled doping concentration, it exhibits a unique ferromagnetic-antiferromagnetic (FM-AFM) coupling. Assisted by theoretical calculations, we demonstrated that FM-AFM coupling presents a strong link to doping contents and doping sites. Wherein, the FM ordering mostly comes from N atoms and the AFM ordering originate from Re atoms. At the N-doping content of 4.24%, the saturated magnetization of N-doped ReS_2 reached the largest value of 2.1 emu g^{-1} at 2 K. Further altering the content to 6.64%, the saturated magnetization of N-doped ReS_2 decreases, but exhibits a distinct exchange bias (EB) phenomenon of around 200 Oe. With controlled N-doping concentrations, the intrinsic spin in ReS_2 could be well altered and resulted in distinct magnetism, presenting tremendous potential for spintronic devices in information storage.

npj 2D Materials and Applications (2018)2:22 ; doi:10.1038/s41699-018-0068-0

INTRODUCTION

Recent years have witnessed the rapid development of transition metal dichalcogenides (TMDs) because of their distinctive electronic, optical, and catalytic properties.[1–3] The spin-orbit coupling and loss of inversion symmetry in TMDs trigger the spin splitting at the valence band maximum, which enables TMDs to be promising for spintronics and nanoelectronic devices.[4] However, further development of TMDs in spintronics was obstructed by their intrinsic nonmagnetic property. Xu et al. held the viewpoint of crystal symmetry dominating the nature of electronic Bloch states and, continuously tuned the orbital magnetic moments of MoS_2,[5,6] which afford opportunity for altering the magnetism of TMDs and realizing the electronic functionalization. Furthermore, lowering the symmetry was reported to introduce interesting magnetic property.[7] Hence, TMDs nanoribbons were predicted to exhibit extraordinary magnetic property due to their asymmetric zigzag- or armchair-terminated edges.[8–11] Unfortunately, the stiff synthesis of TMDs nanoribbons impeded the further experimental investigations on the magnetic property. Among numerous TMDs, ReS_2, a new member of TMDs, stands out due to its strong anisotropy in which both the in and out-of plane anisotropy arrange along lattice vectors.[12,13] Such distinguishing properties surely make ReS_2 attractive for spintronic devices but remain scant, due to the nonmagnetic nature of ReS_2.[14,15]

Chemical doping is known to be an effective and convenient approach to modify the properties of 2D materials, and has been an essential approach for functionalization. Doping TMDs with transition metal atoms has been reported to change electronic properties and enhance the catalytic performance.[16,17] With regard to the magnetic properties of TMDs, doping with heavy metal atoms would result in magnetic agglomeration, which hinders their further functionalization. Meanwhile, some ab initio studies have predicted that doping of non-metal atoms can significantly tune the magnetic properties of TMDs.[14,18] In contrast to the magnetic moment from d-electrons of transition metal atoms, the magnetism based the *sp* states of non-metal elements exhibits no clustering of magnetic ions and stronger long range exchange coupling interactions. Nevertheless, the magnetic effect of non-metal light elements doping in TMDs has been rare experimentally explored. Further, doping with non-metal atoms favors the potential exploitation of ReS_2 in spintronic applications.

We utilized the method of N-doping to introduce magnetic domains into anisotropic ReS_2 lattice, giving rise to a transition from nonmagnetic to tunable magnetic ordering. Both of the experimental and computational results confirmed that the N-doping in ReS_2 prefers to take place at the edge site than in-plane site. By means of tuning nitrogen doping content, the intrinsic spin in ReS_2 could be well altered and, therefore, resulted in an enhanced ferromagnetic-antiferromagnetic (FM-AFM) coupling. Wherein, the FM ordering mostly comes from N atoms and the AFM ordering originate from Re atoms. At the N-doping content of 4.24%, the saturated magnetization reached 2.1 emu g^{-1} at 2 K. Further altering the content to 6.64%, our system exhibited a more distinct exchange bias (EB) of around 200 Oe. Above, N-doped ReS_2, possessing such eminent magnetic properties presents great potential for spintronic devices.

RESULTS AND DISCUSSIONS

To begin with, we investigated the morphology of N-doped ReS_2 utilizing scanning electron microscope (SEM). In Fig. 1a, N-doped ReS_2 exhibited the morphology of uniform nanospheres with

[1]College of Chemistry and Molecular Sciences, Wuhan University, 430072 Wuhan, China; [2]School of Physics and Technology, Wuhan University, 430072 Wuhan, China and [3]National Center for Nanoscience and Technology, 100190 Beijing, China
Correspondence: Lei Fu (leifu@whu.edu.cn)

Received: 6 February 2018 Revised: 24 June 2018 Accepted: 28 June 2018
Published online: 06 August 2018

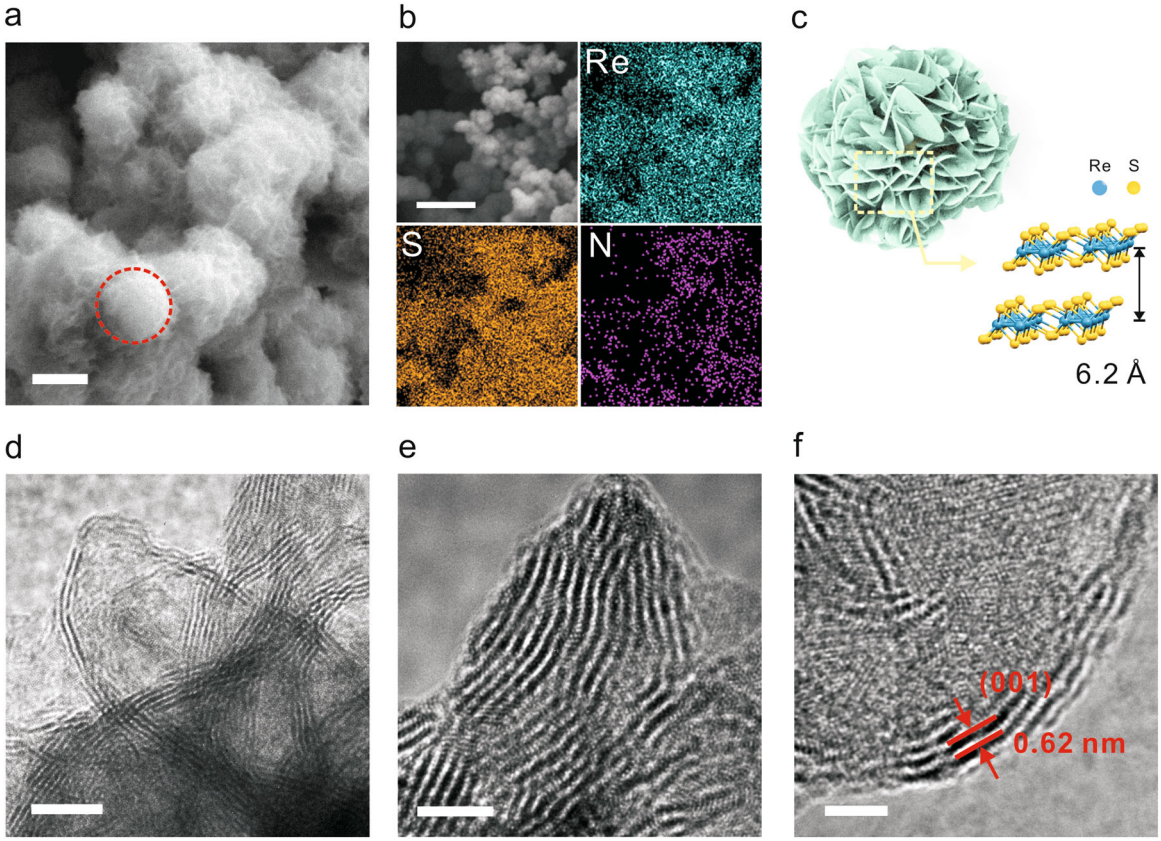

Fig. 1 Morphology characterization of N-doped ReS_2 nanospheres. **a** SEM image of uniformly distributed N-doped ReS_2 nanospheres. The radius approached to 170 nm. Scale bar: 400 nm. **b** EDS mapping of N-doped ReS_2 nanospheres. Scale bar: 1 μm. **c** Schematic illustration of N-doped ReS_2 nanosphere assembled by twisted nanosheets. **d–f** TEM images of N-doped ReS_2 at different magnification. Scale bar: 10 nm, 5 nm, 4 nm. The interlayer distance was measured to be 0.62 nm, corresponding to the (001) plane of ReS_2

subtle structures on the surface. The ReS_2 nanospheres were comprised of woven nanosheets with well exposed edge sites. As showed in Fig. 1b, energy dispersive spectrometer (EDS) analysis demonstrated the elemental information about Re and S, while the overlapped N mapping indicated the homogeneous distribution of the dopants. Figure 1c illustrated the simulated morphology of N-doped ReS_2 with (001) crystal face exposed. High-resolution transmission electron microscopy (HRTEM) was utilized to demonstrate the woven nanosheet of N-doped ReS_2 (Fig. 1d,e), consistent with the morphology shown in the SEM image. In Fig. 1f, the interlayer distance was measured to be 0.62 nm, corresponding to the (001) plane of ReS_2.[19–21]

X-ray photoelectron spectroscopy (XPS) was utilized to examine the elemental compositions and bonding configurations. To evidence the existence of N, commercial ReS_2 powder was also characterized as a comparison object. In Fig. S1, N 1 s XPS pattern did not show any signal peak. To alter the magnetism of N-doped ReS_2, three samples with different N-doping contents were prepared; the levels of doping were regulated by the stoichiometric ratio of reaction precursors (Table S1 in supplementary material). XPS analysis demonstrated that the nitrogen concentrations in the prepared samples were 2.20, 4.24, and 6.64 at.%, while $ReN_{2.20}$, $ReN_{4.24}$, $ReN_{6.64}$ were used for identification, respectively. The N 1 s XPS pattern of $ReN_{2.20}$ in Fig. 2a only exhibited only one peak with the binding energy near 400.0 eV. As the doping content increased to 4.24 at.%, another peak appeared and was measured to be around 397.5 eV (Fig. 2b), corresponding to the binding energy of Re_3N (397.6 eV) in the previous report.[22] Further increasing the nitrogen content to 6.64 at.%, as showed in Fig. 2c, the peak area of Re_3N at 397.5 eV was enlarged. Explicitly, N-doped ReS_2 exhibited two distinct peaks of N 1 s pattern, corresponding to two types of Re–N bonding configurations. In pristine ReS_2, each S atom is bonded to 3 Re atoms. Hence, we postulated the existence of two types of doping sites, i.e., the in-plane site Re_3N (bonding with 3 Re atoms) and the edge site Re_2N – (bonding with 2 Re atoms). As the statistical result presented in Fig. 2d, the peak area ratio of in-plane site Re_3N was employed to confirm the rise of nitrogen concentration, and the value increasing from 19.87% to 24.90% indicated the gradual substitution of nitrogen for in-plane sites. Then, patterns of Re $4f_{5/2}$ (41.8 ~ 42.5 eV) and Re $4f_{7/2}$ (44.2 ~ 44.7 eV) were clearly presented in Fig. 2e, which was consistent with the previous report.[19] Obviously, slight shifts of Re $4f_{5/2}$ and $4f_{7/2}$ peaks witnessed the progressively increasing nitrogen contents in ReS_2 lattice, resulting from the valence state change of Re atoms.

Bader charge analysis in Table 1 indicated the charge transfer to N atoms from the neighboring Re atoms and presented in Fig. 2f, the charges on N atoms at the in-plane sites increased from 6.2392 e to 6.2565 e, representing the electron accepting of N atoms. The charges on N atom at the edge site exhibited a much larger value of 6.4368 e. Meanwhile, it was preferential for nitrogen to substitute the edge sites than the in-plane sites, where the former (0.0936 eV) one possessed a much smaller substitutional energy than that of the latter (0.1296 eV) one. Accordingly, the N 1 s XPS pattern of $ReN_{2.20}$ with only one peak might correspond to the preferential edge doping sites. Afterwards, the edge Re_2N–sites became saturated upon increasing nitrogen contents, allowing N to penetrate into the in-plane sites. The substitutional energy of 2N and 3 N doping were calculated to be 0.0657 eV and 0.0990 eV, respectively, further confirming the above mentioned doping procedure. We consider that the energy barrier of 1 N will restrict the subsequent doping of 2 N and 3 N. In our work, we regulated

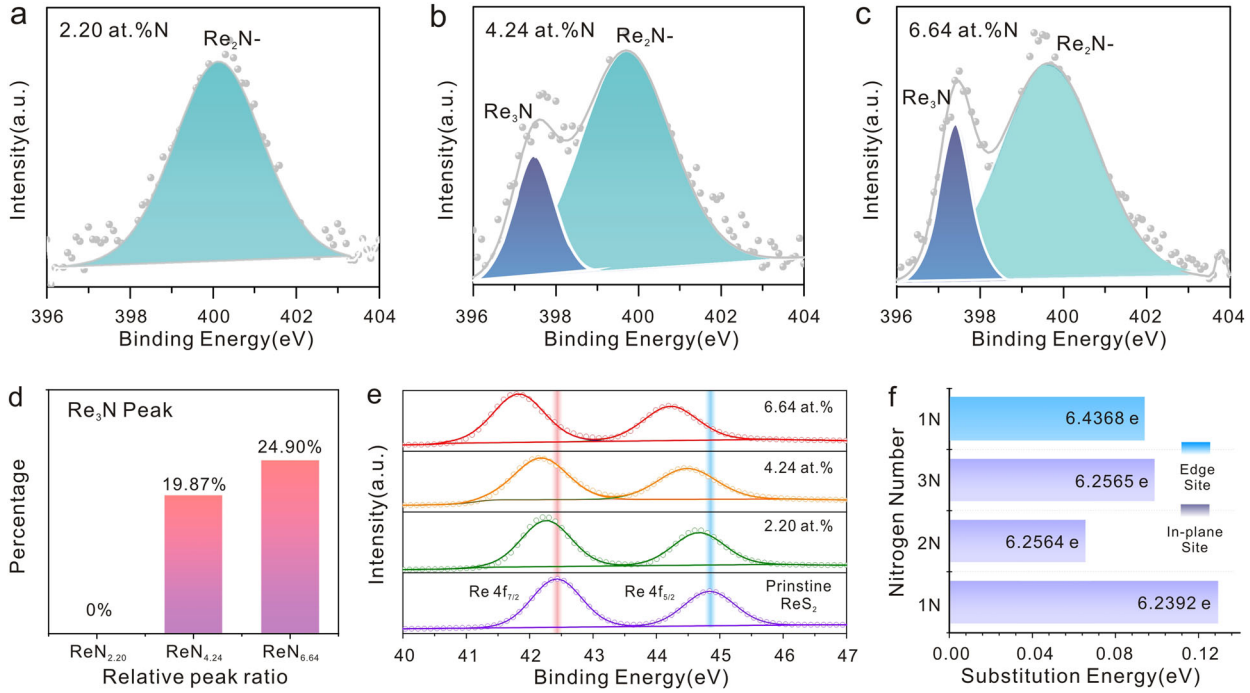

Fig. 2 XPS characterization of pristine ReS_2 and N-doped ReS_2 with different nitrogen doping concentrations. **a–c** N 1 s XPS patterns of N-doped ReS_2 with different nitrogen contents, 2.20, 4.24, and 6.64 at.%, respectively. The XPS pattern of $ReN_{2.20}$ exhibits only one peak with the binding energy near 400.0 eV. When the doping content increased, another peak appeared and was found around 397.5 eV. **d** The statistical analysis of the peak ratio for Re_3N state. The increasing peak ratio of in-plane site Re_3N confirms the rise of nitrogen concentration, indicating the gradual substitution at the in-plane sites. **e** Re 4f XPS patterns of pristine and N-doped ReS_2. There exhibit slight shifts of Re $4f_{5/2}$ and $4f_{7/2}$ peaks which witnessed the progressively increasing nitrogen contents. **f** Bader charge analysis of N-doped ReS_2 in different doping contents and sites

Table 1. Bader charge analysis of pristine ReS_2 and N-doped ReS_2 with different doping contents and sites

Model	Substitutional energy (eV)	Total magnetic moment (μ_B)	Bader charge (e)
Pristine ReS_2	–	0	–
Edge Sites	0.0936	0.9911	6.4368
1N	0.1296	0.9992	6.2392
2N	0.0657	2.0004	6.2564
3N	0.0990	0.9998	6.2565

Magnetic moment per cell (in μ_B), to the dopant obtained from the Bader charge analysis, substitution energy of N atom (in eV) and Bader charge of N atom (in eV) calculated for different concentrations of nitrogen contents in N doped ReS_2. The charges on N atoms at the in-plane sites increased from 6.2392 e to 6.2565 e, representing the electron accepting of N atoms. The charges on N atom at the edge site exhibited a much larger value of 6.4368 e. Meanwhile, it was preferential for nitrogen to substitute the edge sites than the in-plane sites, where the former (0.0936 eV) one possessed a smaller substitutional energy than the latter (0.1296 eV), agree well with the XPS results

the doping contents by controlling the ratio of the precursors. According to our experiment results, when the doping contents less than 2.20%, the doping at edge site is dominant. However, when the doping content is 4.24% and above, the peak area reveal the dominant role of doping at in-plane sites. And this helps explain the lower substitutional energy of 2N and 3N. In addition, S 2p states of ReS_2 with various nitrogen contents presented no obvious change in peak position (Fig. S2a in supplementary material). The corresponding XPS spectra in the whole range were also displayed in Fig. S2b–d (Supplementary material).

To detect the magnetism variation of N-doped ReS_2, temperature evolution of mass magnetic susceptibility (χ_{mass}) was adopted. Commercial ReS_2 powder exhibited no apparent response to the external magnetic field, while the χ_{mass} value of $ReN_{4.24}$ increased 100 times compared to the pristine one, due to the introduction of local magnetic domain induced by nitrogen doping (Fig. 3a). Figure 3b–d displayed the χ_{mass} measured for $ReN_{2.20}$, $ReN_{4.24}$, and $ReN_{6.64}$ with the temperature evolution (0~150 K) of field cooling (FC) and zero field cooling (ZFC). The insets in the left pane demonstrated the corresponding integrated ZFC/FC curves. The whole ZFC/FC curves of commercial ReS_2 powder were shown in Fig. S3 (supplementary material). Due to the amorphous structure of commercial ReS_2, the non-constant mass susceptibility could be negligible and ought to be induced by weak FM state localized at the edge.[23] In Fig. 3b, the ZFC/FC curves brought out the paramagnetic symptom in which they greatly increased upon lowering the temperature. Evidently, ZFC/FC curves were totally dispersed during the temperature evolution as a result of FM-AFM coupling.[24] Furthermore, with the increasing N-doping content, there existed small protuberances around 57 K corresponding to the Néel point (T_N), which was the consequence of AFM forces (Fig. 3c,d).[25] Once lowering the temperature under the Néel point, the decreasing trend of χ_{mass} exhibited the dominated AFM, thus leading to the formation of protuberance. The presence of the protuberance in both $ReN_{4.24}$ and $ReN_{6.64}$ but not in $ReN_{2.20}$ confirmed that doping contents had greatly influenced the partial spin electrons of ReS_2. Lowering the temperature to 2 K, the partial spin electrons had totally twirled along the external field, the consequence of which was the enormously increased of χ_{mass}. As intuitional magnetic property was a mixture of various interactions within a magnet,[26,27]

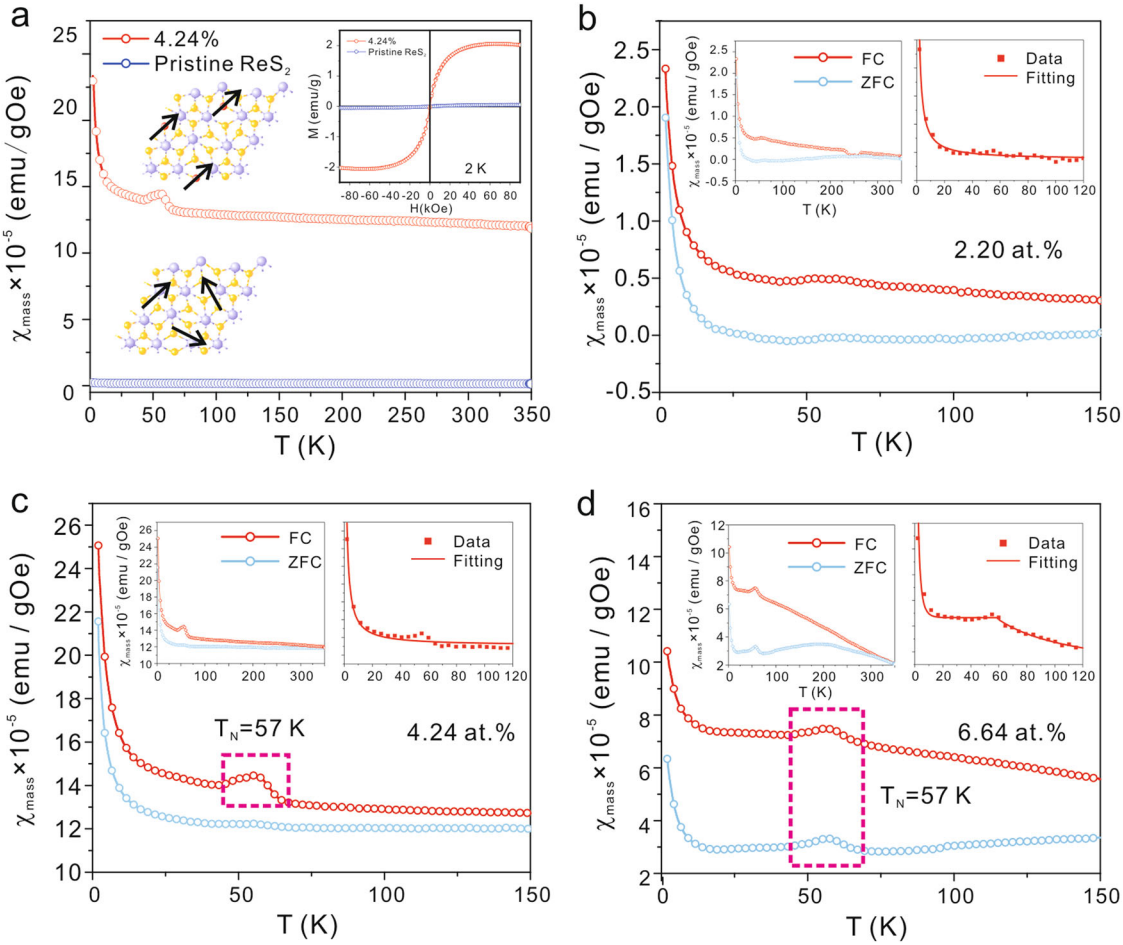

Fig. 3 ZFC/FC curves of pristine ReS_2 and N-doped ReS_2 with different nitrogen doping concentrations. **a** FC curves of pristine ReS_2 and $ReN_{4.24}$ with the maximal saturated magnetization. The inset was their hysteresis loops at 2 K. **b**–**d** FC and ZFC curves between 0 K and 150 K at different N-doping levels, 2.20, 4.24, and 6.64 at.%, respectively. The insets showed the ZFC/FC curves in complete temperature range and their fitted data assuming the temperature from 0 K to 120 K, where Curie–Weiss law and Brillouin function were employed. The Néel point was around 57 K

especially for doped materials. As the AFM force was clearly shown in the ZFC/FC curves, here, the contribution from other two sorts of magnetism was rather important. In order to distribute the magnetic response in paramagnetic and ferromagnetic form to study the FM forces in N-doped ReS_2, the χ_{mass} versus temperature profile of different samples was fitted assuming the two contributions, i.e., paramagnetic following the Curie–Weiss law at high temperature and ferromagnetic obeying Brillouin function at low temperatures within the mean field approximation (see insets in the right pane of Fig. 3b–d).[28,29] The fitting process had utilized FC curves ranging from 0 to 120 K as primitive data. As a result, $ReN_{2.20}$ and $ReN_{4.24}$ matched well with Curie law at 0~120 K (Fig. 3b,c), whereas in the $ReN_{6.64}$ sample, the fit yields the angular momentum number $J \approx 0.1$ as an average value over all the samples at 0~60 K, indicating the strongest ferromagnetism in $ReN_{6.64}$ (Fig. 3d). At 60~120 K, $ReN_{6.64}$ also matched well with the Curie-Weiss function, which represented the paramagnetic part. It should be noted that the N-doping concentration in this work was 2–6%, while the number of magnetic centers increased upon raising the level of N-doping. However, N-doping at such levels would not introduce much magnetic interaction and the induced magnetic centers were far from each other, which hindered the formation of long-range magnetic ordering.[26] To exclude the effect of 3d block metal impurities on the magnetic properties of N-doped ReS_2, such as Zn, Cr, Mn, Fe, Co, and Ni, inductively coupled plasma mass spectrometry (ICP-MS) was utilized and presented in Table S2 (supplementary material). As a result, the total magnetic susceptibility of 3d-block metals was below 10^{-8} emu g^{-1} Oe^{-1} at 0 K and in 1 kOe field. As χ_{mass} values for N-doped ReS_2 reached orders from 10^{-4} down to 10^{-5} emu g^{-1} Oe^{-1} in 1 kOe field, the contribution of Fe, Ni, Co, and Mn was thought to be negligible in measurements of temperature evolution of χ_{mass} and hysteresis loops, thus absolutely not covering the magnetic properties of N-doped ReS_2. As a result, the total magnetic susceptibility of 3d-block metals was thought to be negligible in magnetism measurements.To further study the magnetism of N-doped ReS_2, the hysteresis loops were employed and exhibited in Fig. 4a. At the lowest temperature (2 K) where the whole spin twirled, $ReN_{4.24}$ possessed the largest saturated magnetization of 2.1 emu g^{-1}, while $ReN_{6.64}$ possessed a smaller saturated magnetization of 1.5 emu g^{-1}. The computational results in Table 1 revealed that the magnetic moment of 3 N atom doped configuration was 0.9998 μ_B, which was much less than that of 2 N atom doped configuration (2.0004 μ_B). It could be explained that $ReN_{6.64}$ had lost much in-plane magnetic moment than $ReN_{4.24}$, leading to a decrease in saturated magnetization.

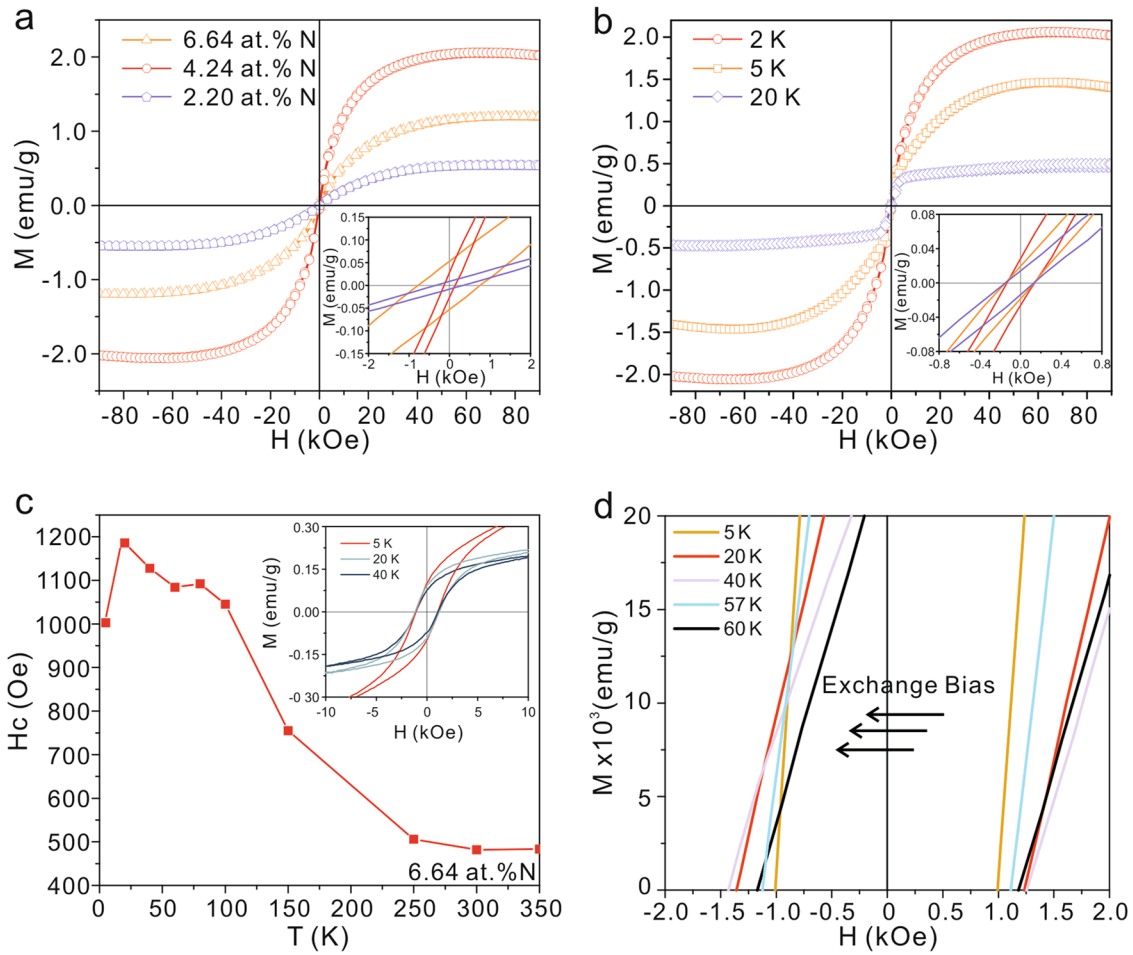

Fig. 4 Hysteresis loops of ReN_x with different nitrogen doping concentrations and detailed analysis with temperature evolution. **a** Hysteresis loops of ReN_x at 2 K, the inset showed the non-zero coercivity around the origin. **b** Hysteresis loops of $ReN_{4.24}$ at certain temperatures. **c** Temperature evolution of coercivity (H_c) of the $ReN_{6.64}$ sample. The inset showed the exchange bias around the Néel point. **d** Magnified view of the hysteresis loops of $ReN_{6.64}$ at the temperature of 5 K, 20 K, 40 K, 57 K, 60 K, respectively

The inset in Fig. 4a showed the non-zero coercivity of different samples, indicating the emergence of magnetic anisotropy in ReS_2 lattice triggered by nitrogen doping. Therein, $ReN_{6.64}$ possessed the strongest coercivity of ≈1300 Oe and therefore possessed the strongest ferromagnetism. Figure 4b exhibited hysteresis loops of $ReN_{4.24}$ at 2 K, 5 K, and 20 K, which possessed the largest saturated magnetization. Lowering the temperature below Néel point, the saturated magnetization began escalating rapidly due to spin flip.[30] To obtain the coercivity in $ReN_{6.64}$, we utilized the formula: $H_c = (H_1 - H_2)/2$, where H_1 was the x-intercept of the positive axis and H_2 was the negative one.[31] Fig. 4c displayed the temperature evolution of coercivity in $ReN_{6.64}$, in which the coercivity augmented at lower temperature, showing the ferromagnetism feature. In the inset of Fig. 4c, we observed an obvious EB caused by FM-AFM coupling. To magnify, Fig. 4d clearly displayed that the coercivity of $ReN_{6.64}$ deviated ≈200 Oe from the origin at 40 K and 20 K, demonstrating the fairly strong EB in $ReN_{6.64}$. The temperature exceeding 40 K, the EB disappeared owing to thermal disturbance. Under 20 K, the EB vanished as well, due to all the spin electrons in the same orientation under an external field.

To better comprehend the unique magnetic behavior of N-doped ReS_2, spin-polarized density functional calculations (DFT) were performed in the Vienna ab initio simulation package (VASP).[14,32–34] To figure out the correlation between doping contents and magnetic distribution, the magnetic moment and charge distribution of the supercell comprised of 48 atoms had been presented in Fig. 5. The computational models were presented in Fig. S4. Since the magnetic properties exhibited a strong dependence on the nitrogen content, the substitutional doping was modeled by replacing S atoms by N atoms, considering the experimentally and computationally nitrogen concentration to be followed closely. The nitrogen concentrations from 1N to 3N were calculated to be 2.08, 4.17, and 6.25 at.%, respectively, resulting from the size of the supercell employed in the calculations. As showed in Fig. 5a–c, the most stabilized structures exhibited FM ordering with 0.703, 1.522, and 0.714 μ_B magnetic moment per supercell for 1N, 2N, and 3N, respectively. The distribution of magnetic moment in μ_B for various nitrogen concentrations was listed in Table S2–4 (supplementary material). At the nitrogen content of 2N, the $ReN_{4.17}$ exhibited a largest total magnetic moment compared to the $ReN_{2.08}$ and $ReN_{6.25}$, consistent with the experimental results presented in Fig. 3. Wherein, 60% magnetic moments came from N atoms but only ~40% came from Re atoms. As for the contribution of orbitals, *s*, *p*, and *d* orbital could attribute unevenly, where, the total magnetic moment of $ReN_{4.17}$ was 1.522 μ_B (0.051 μ_B came from *s* orbital, 0.858 μ_B came from *p* orbital and 0.612 μ_B came from *d* orbital), as presented in Table S3. Notably, the AFM moment mostly originated from 5*d* orbital of Re atoms.

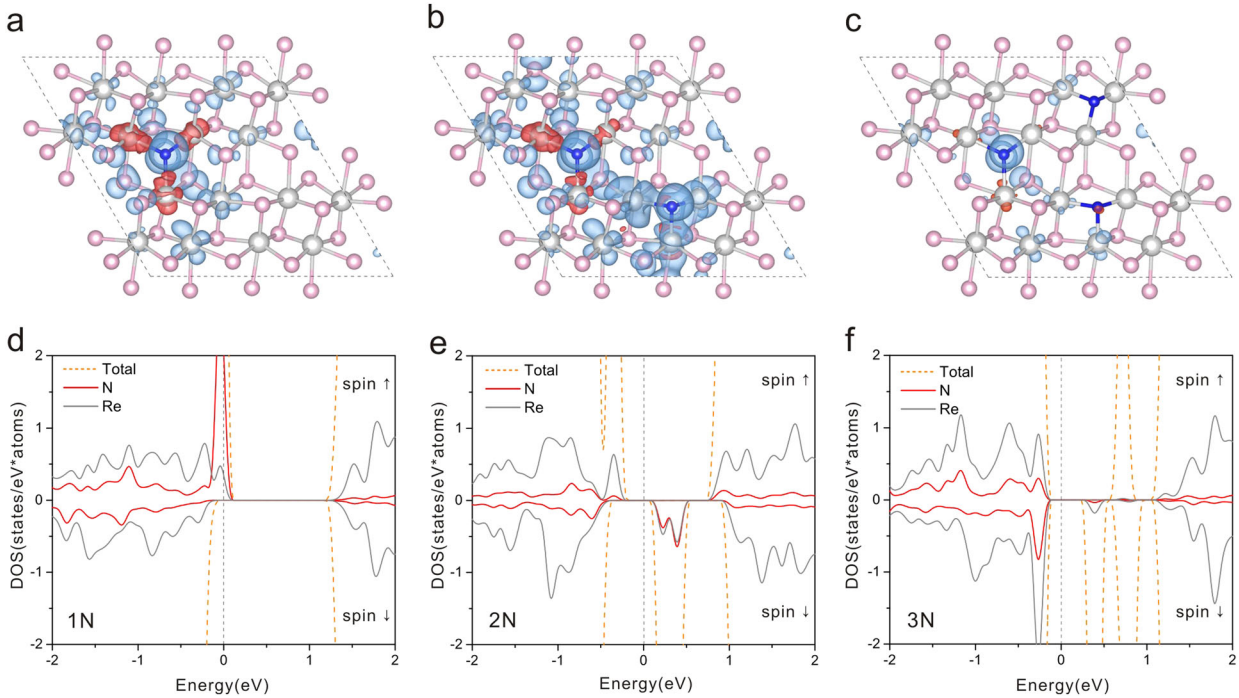

Fig. 5 Computational simulation of ReN_x doped with 1N, 2N, and 3N. **a**–**c** The configuration view of ReN_x, with positive (negative) spin densities plotted in blue (red) for isosurfaces at 1×10^{-3} e Å^{-3}. **d**–**f** The corresponding DOS plots of ReS_2 doped with 1N, 2N, and 3N, respectively

The density of state (DOS) plots, as presented in Fig. 5d−f, demonstrated the spin electronic features and the exchange coupling regulated by the conduction electrons. The spin-polarized electronic features at the Fermi level in the DOS plots exhibited different contributions from both N and the neighboring Re atoms. In Fig. 5d, the predominant contribution came from the N atom, presenting a spin-up channel of electrons at the Fermi level and agree well with the ferromagnetism ordering of $ReN_{4.24}$ observed in Fig. 3b. Both of Fig. 5e,f revealed the dominant contribution from Re atoms near the Fermi level. Figure 5e exhibited a spin-up channel near the Fermi level, while the Fig. 5f shown an opposite channel. Namely, magnetic configurations, in most possible, demonstrated a varying effective magnetic moment per cell and exhibited both AFM and FM behavior. This could explain the emergence of the EB phenomenon discussed in the previous section. Moreover, with the increase in nitrogen content, robust mid-gap states near the Fermi levels emerged in Fig. 5e,f, suggesting that the electrons could conduct along the Re chains by hopping. In this way, the formation of both FM and AFM magnetic domain was due to appear, thus causing the relatively strong EB phenomenon. Under a certain condition where the temperature was extremely low (2 K) and the external field was relatively high (1 kOe), the spin electrons in ReN_x would totally flip to cater the external field.

In conclusion, we utilized the method of non-metal doping (N) in ReS_2 and found an obvious magnetic transition from nonmagnetic to magnetic ordering. Both of the experimental results and computational simulations confirmed that the N-doping in ReS_2 prefers to take place at the edge sites than in-plane sites, where the former one induces localized FM states. Experimentally, at the N-doping content of 4.24%, the saturated magnetization reached 2.1 emu g^{-1} at 2 K. Further altering the content to 6.64%, our system exhibits a distinct exchange bias phenomenon of around 200 Oe. Taking orbital contribution into account, we observed that the FM moment mostly generated from 2*p* orbital of N atom while the AFM moment mostly originated from 5*d* orbital of Re atom. The superior magnetic properties could be attributed to the redistribution of electrons after nitrogen doping. Ultimately, N-doped ReS_2 with high coercivity and exchange bias had shown enormous potential for spintronic devices. The strong in and out-of plane anisotropy of ReS_2 also allow it attractive for spintronic devices and thus promise N-doped ReS_2 a bright future for spintronics.

METHODS

Synthesis of N-doped ReS_2

Ammonium perrhenate NH_4ReO_4 (99.999%, Alfa Aesar) and thiourea (99%, SCR, China) were used as precursors for hydrothermal reaction, which were dissolved in 15 mL deionized water (DI) with a certain molar ratio. Then the mixture was ultrasonic dispersed for 5 min and then transferred to a 25 mL polytetrafluoroethylene (PTFE) container with a stainless steel autoclave. It was kept in a drying oven at the temperature of 200 °C for 24 h. After that, the product was gradually washed by DI and ethanol. Finally, the ReS_2 nanospheres were obtained after a freeze-drying process for 12 h.

Material characterizations

Raman spectroscopy was performed in a laser micro-Raman spectrometer (Renishaw in Via, 532 nm excitation wavelength). Scanning electron microscopy (SEM) images were performed in a ZEISS Merlin Compact SEM and energy dispersive X-ray spectroscopy (EDX) was collected using an INCAPentalFETx3 Oxford EDX. Transmission electron microscope (TEM) images were performed in a JEM-2100 TEM (JEOL Ltd.) under the acceleration voltage of 200 kV.

Magnetization measurements

Physical property measurement system (PPMS) equipped with a vibrating sample magnetometer (VSM) from Quantum Design, U.S.A. was used to conduct magnetization measurements of N-doped ReS_2 samples. Hysteresis loops were measured under the temperature ranging from 2 to 350 K and in the static external magnetic fields range from −90 to + 90 kOe.

Temperature profiles of the mass magnetic susceptibility, χ_{mass}, were measured in a sweep mode up to a field of 1 kOe in a temperature range between 5 and 300 K. Magnetization values were corrected by substracting background signals from sample holder, sample capsule, and respective Pascal constants. The magnetic impurity elements (such as Zn, Cr, Co, Fe, Ni, Mn) of the sample are below 10 ppm measured by ICP spectrometry (Thermo Scientific iCAP−Q).

Structural model

The optimized lattice parameters for the monolayer ReS_2 are 6.41 Å × 6.52 Å with angle 91.8°, in very good consistency with the experimental value. The periodically repeated 2 × 2 supercell were applied comprising 48 atoms. A vacuum layer of 12 Å perpendicular to the sheet was applied to avoid the interaction between the repeated images. For edge doping model, in addition, we add vacuum layer to nearly 23.0 Å along one plane axis. Substitutional doping was modeled by replacing sulfur by nitrogen atoms in the pristine ReS_2 supercell.

The formation energy E_f of the doped complexes was calculated according to the following formula:

$$E_f = 1/n(E_{ReN} - E_{ReS_2} + n(\mu_N - \mu_S))$$

where E_{ReN} and E_{ReS_2} stand for the total energy of the doped and pristine ReS_2 sheet, respectively, μ is the chemical potential of N and S atoms (here approximated by the atomic energies of N and S), and n is the number of substituted atoms.

Computational methods

All calculations under periodic boundary conditions were carried out using the Vienna ab initio simulation package (VASP). Electron–ion interactions were dealt with by the projector-augmented wave (PAW) method with the encut energy of plane-wave up to 450 eV. Electronic exchange and correlation potential were described in a generalized gradient approximation (GGA) with the functional of Perdew, Burke, and Ernzerhof (PBE) with spin taken into account. During optimizations for adsorption models and bulk doping models (edge doping model), the Brillouin zone was sampled using a 3 × 3 × 1 (3 × 1 × 1) Monkhorst-pack k-point mesh and Gaussian smearing of 0.1 eV. The relaxations are converged until the residual atomic forces adjusted by conjugate gradient algorithm were lower than 0.02 eV $Å^{-1}$ and the total energies difference between successive iteration steps were smaller than 10^{-5} eV. The distribution of electron density was calculated with a denser grid of 7 × 7 × 1 *k*-point mesh and Gaussian smearing of 0.01 eV. In addition, the partitioning of the ground-state electronic density into contributions projected to the different atoms was performed by means of Bader analysis. Electronic densities of states were calculated using the tetrahedron method at a denser 9 × 9 × 1 *k*-point mesh. Magnetic moments were calculated from the difference between the numbers of electrons in occupied majority-spin and minority-spin states. Local magnetic moments were calculated by projecting the plane-wave components of all occupied eigenstates onto spherical waves inside an atomic sphere and integrating the resulting local density of states.

Data availability

The datasets generated during and/or analyzed during the current study are available from the corresponding author on reasonable request.

ACKNOWLEDGEMENTS

The research was supported by the National Natural Science Foundation of China (Grants 21673161 and 21473124) and the Sino-German Center for Research Promotion (Grant 1400).

AUTHOR CONTRIBUTIONS

L.F. developed the concept and conceived the experiments. Q.Z. and Z.M.R. carried out the experiments and wrote the manuscript, contributing equally to this manuscript. L.F., Q.Z., Z.M.R., N.W., W.J.W., Y.J.G., Q.Q.Z., X.N.S., L.Z., and J.S. contributed to data analysis and scientific discussion.

ADDITIONAL INFORMATION

Supplementary information accompanies the paper on the *npj 2D Materials and Applications* website (https://doi.org/10.1038/s41699-018-0068-0).

Competing interests: The authors declare no competing interests.

Publisher's note: Springer Nature remains neutral with regard to jurisdictional claims in published maps and institutional affiliations.

REFERENCES

1. Li, Y., Wang, H., Xie, L., Liang, Y., Hong, G. & Dai, H. MoS_2 nanoparticles grown on graphene: an advanced catalyst for the hydrogen evolution reaction. *J. Am. Chem. Soc.* **133**, 7296–7299 (2011).
2. Mak, K. F., He, K. L., Shan, J. & Heinz, T. F. Control of valley polarization in monolayer MoS_2 by optical helicity. *Nat. Nanotech.* **7**, 494–498 (2012).
3. Xie, J. et al. Defect-rich MoS_2 ultrathin nanosheets with additional active edge sites for enhanced electrocatalytic hydrogen evolution. *Adv. Mater.* **25**, 5807–5813 (2013).
4. Zhu, Z. Y., Cheng, Y. C. & Schwingenschlögl, U. Giant spin-orbit-induced spin splitting in two-dimensional transition-metal dichalcogenide semiconductors. *Phys. Rev. B* **84**, 153402 (2011).
5. Wu, S. F. et al. Electrical tuning of valley magnetic moment through symmetry control in bilayer MoS_2. *Nat. Phys.* **9**, 149–153 (2013).
6. Feng, N., Mi, W., Cheng, Y., Guo, Z., Schwingenschlogl, U. & Bai, H. First principles prediction of the magnetic properties of Fe-X_6 (X = S, C, N, O, F) doped monolayer MoS_2. *Sci. Rep.* **4**, 3987 (2014).
7. Hoffmann, A. Symmetry driven irreversibilities at ferromagnetic-antiferromagnetic interfaces. *Phys. Rev. Lett.* **93**, 097203 (2004).
8. Pan, H. & Zhang, Y. W. Edge-dependent structural, electronic and magnetic properties of MoS_2 nanoribbons. *J. Mater. Chem.* **22**, 7280–7290 (2012).
9. Li, Y., Zhou, Z., Zhang, S. & Chen, Z. MoS_2 nanoribbons: high stability and unusual electronic and magnetic properties. *J. Am. Chem. Soc.* **130**, 16739–16744 (2008).
10. Zhang, H., Li, X. B. & Liu, L. M. Tunable electronic and magnetic properties of WS_2 nanoribbons. *J. Appl. Phys.* **114**, 093710 (2013).
11. Pan, H. & Zhang, Y. W. Tuning the electronic and magnetic properties of MoS_2 nanoribbons by strain engineering. *J. Phys. Chem. C.* **116**, 11752–11757 (2012).
12. Rahman, M., Davey, K. & Qiao, S. Z. Advent of 2D rhenium disulfide (ReS_2): fundamentals to applications. *Adv. Funct. Mater.* **27**, 1606129 (2017).
13. Zhang, X. & Li, Q. Electronic and magnetic properties of nonmetal atoms adsorbed ReS_2 monolayers. *J. Appl. Phys.* **118**, 064306 (2015).
14. Cakir, D., Sahin, H. & Peeters, F. M. Doping of rhenium disulfide monolayers: a systematic first principles study. *Phys. Chem. Chem. Phys.* **16**, 16771–16779 (2014).
15. Qu, Y., Pan, H. & Kwok, C. T. Hydrogenation-controlled phase transition on two-dimensional transition metal dichalcogenides and their unique physical and catalytic properties. *Sci. Rep.* **6**, 34186 (2016).
16. Suh, J. et al. Doping against the native propensity of MoS_2: degenerate hole doping by cation substitution. *Nano. Lett.* **14**, 6976–6982 (2014).
17. Zhou, W. J. et al. MoO_2 nanobelts@nitrogen self-doped MoS_2 nanosheets as effective electrocatalysts for hydrogen evolution reaction. *J. Mater. Chem. A* **2**, 11358–11364 (2014).
18. Dolui, K., Rungger, I., Pemmaraju, C. D. & Sanvito, S. Possible doping strategies for MoS_2 monolayers: an ab initio study. *Phys. Rev. B* **88**, 075420 (2013).
19. Zhang, Q. et al. Extremely Weak van der waals coupling in vertical ReS_2 nanowalls for high-current-density lithium-ion batteries. *Adv. Mater.* **28**, 2616–2623 (2016).
20. Zhang, Q., Wang, W. J., Zhang, J. Q., Zhu, X. H. & Fu, L. Thermally induced bending of ReS_2 nanowalls. *Adv. Mater.* **30**, 1704585 (2018).
21. Zhang, Q. et al. Edge-to-edge oriented self-assembly of ReS_2 nanoflakes. *J. Am. Chem. Soc.* **138**, 11101–11104 (2016).
22. Soto, G., Rosas, A., Farias, M. H., De, la Cruz, W. & Diaz, J. A. Characterization of rhenium nitride films produced by reactive pulsed laser deposition. *Mater. Character* **58**, 519–526 (2007).
23. Ouyang, F., Yang, Z., Ni, X., Wu, N., Chen, Y. & Xiong, X. Hydrogenation-induced edge magnetization in armchair MoS_2 nanoribbon and electric field effects. *Appl. Phys. Lett.* **104**, 071901 (2014).
24. Nakamura, K., Kato, Y., Akiyama, T., Ito, T. & Freeman, A. J. Half-metallic exchange bias ferromagnetic/antiferromagnetic interfaces in transition-metal chalcogenides. *Phys. Rev. Lett.* **96**, 047206 (2006).
25. Haldane, F. D. M. Nonlinear field theory of large-spin heisenberg antiferromagnets: semiclassically quantized solitons of the one-dimensional Easy-Axis Néel state. *Phys. Rev. Lett.* **50**, 1153–1156 (1983).
26. Blonski, P. et al. Doping with graphitic nitrogen triggers ferromagnetism in graphene. *J. Am. Chem. Soc.* **139**, 3171–3180 (2017).
27. Brinkman, A. et al. Magnetic effects at the interface between non-magnetic oxides. *Nat. Mater.* **6**, 493–496 (2007).
28. Viehland, D., Jang, S. J., Cross, L. E. & Wuttig, M. Deviation from Curie-Weiss behavior in relaxor ferroelectrics. *Phys. Rev. B* **46**, 8003–8006 (1992).

29. Tucek, J. et al. Sulfur doping induces strong ferromagnetic ordering in graphene: effect of concentration and substitution mechanism. *Adv. Mater.* **28**, 5045–5053 (2016).
30. Shima, T., Hampel, F. & Gladysz, J. A. Molecular gyroscopes: $\{Fe(CO)_3\}$ and $\{Fe(CO)_2(NO)\}+$ rotators encased in three-spoke stators; facile assembly by alkene metatheses. *Angew. Chem. Int. Ed.* **43**, 5537–5540 (2004).
31. Gilbert, D. A. et al. Controllable positive exchange bias via redox-driven oxygen migration. *Nat. Commun.* **7**, 11050 (2016).
32. Loh, G. C. & Pandey, R. Robust magnetic domains in fluorinated ReS_2 monolayer. *Phys. Chem. Chem. Phys.* **17**, 18843–18853 (2015).
33. Zhou, J., Wang, Q., Sun, Q. & Jena, P. Intrinsic ferromagnetism in two-dimensional carbon structures: triangular graphene nanoflakes linked by carbon chains. *Phys. Rev. B* **84**, 081402 (2011).
34. Li, X. & Wang, Q. Tunable ferromagnetism in assembled two dimensional triangular graphene nanoflakes. *Phys. Chem. Chem. Phys.* **14**, 2065–2069 (2012).